

Magnetohydrodynamic activity inside a sphere

Pablo D. Mininni¹ and David C. Montgomery²

¹ National Center for Atmospheric Research, P.O. Box 3000, Boulder, Colorado 80307 and

² Dept. of Physics and Astronomy, Dartmouth College, Hanover, NH 03755

(Dated: November 4, 2019)

We present a computational method to solve the magnetohydrodynamic equations in spherical geometry. The technique is wholly spectral and uses an expansion basis that is adapted to the geometry: the Chandrasekhar-Kendall vector eigenfunctions of the curl. In this work, simulations for isolated spheres are presented, although different boundary conditions can be studied using the same method. The intent is to be able to study those aspects of the nonlinear dynamical evolution that are affected by the spherical geometry at moderate Reynolds number. The parallel code preserves with high accuracy the ideal invariants of the system. Examples of results for selective decay and dynamo simulations are discussed. In dynamo simulations, spontaneous flips in the direction of the magnetic field are observed.

PACS numbers: 47.11.-j; 47.11.Kb; 91.25.Cw; 95.30.Qd

I. INTRODUCTION

Magnetohydrodynamic “dynamo” processes are those in which the motions of an electrically conducting fluid amplify and maintain a finite magnetic field, starting from an arbitrarily small one. They have long been of interest for geophysics and astrophysics [1, 2, 3, 4, 5, 6], and have more recently become of interest with regard to laboratory attempts to generate dynamo magnetic fields in liquid metals [7, 8, 9, 10, 11, 12]. The relevant theoretical and computational literature is vast, and extensive reviews have recently been given (see e.g. Refs. [4, 13, 14, 15]).

In our own work, we have lately been studying dynamo processes numerically, using turbulent three-dimensional magnetohydrodynamic (hereafter, “MHD”) codes of the familiar Orszag-Patterson pseudospectral variety [16, 17, 18, 19, 20]. Such codes treat homogeneous turbulence efficiently, but are mainly useful in situations involving spatially periodic boundary conditions. Particularly for the case of planetary dynamos and laboratory experiments, restrictions to periodic boundary conditions are a severe limitation. Essential ingredients, such as rotation, global angular momentum, and the interfaces between conducting and non-conducting regions are not readily included. It is to be expected that all of these play a role in the physical situations of interest, and give rise to qualitatively new physical processes not accessible with periodic boundaries.

This present paper represents our attempt to begin a study of these processes by introducing, and displaying some results from, a computational method that is adapted to the geometry of isolated spheres. Our goal is not to reach realistic geophysical parameter regimes (out of the question for the foreseeable future, in any case), but rather to isolate and study those new physical processes that appear in this geometrically more realistic setting. Our efforts are to be distinguished from such impressive geo-dynamo computations as those of Glatzmaier and Roberts (e.g. Refs. [2, 21]), the goal of which

has been and is the reproduction of observational characteristics of the magnetic field of the Earth. Such computations must resort to modeling some of the processes involved in order to cope with the necessarily coarse resolution. We will consider it to be no limitation on our present computations if we are unable to reach realistic geophysical Reynolds numbers, for example. We think of these efforts as studies of MHD dynamo behavior in spherical geometry somewhat in the abstract, with an emphasis on flexibility and clarity, and intending to examine effects that have not been explored in this way before.

The technique is wholly spectral, using an expansion basis that is specifically adapted to spherical geometry: the Chandrasekhar-Kendall (hereafter, “C-K”) vector eigenfunctions of the curl [22, 23, 24, 25, 26]. We believe these to be complete for solenoidal vector functions, but a proof has only been given for the cylindrical case [25]. Some years ago, we found C-K functions to be useful for computing nonlinear MHD behavior inside a conducting periodic cylinder and for studying processes believed to be involved in disruptions of fusion confinement devices [27, 28, 29, 30, 31]. Their advantages lie mainly in their natural geometrical relation to processes that can go on in the specific geometries to which they are adapted, and in the fact that boundary conditions can be built into the individual expansion functions themselves, and so require no further numerical effort to enforce. It will be noticed that far more periodic Fourier coefficients would be necessary, for example, to resolve the processes we will exhibit than coefficients required by the C-K Galerkin expansion. The principal disadvantage is that the size of the convolution sums generated by the nonlinear terms in the MHD equations grows rapidly with the resolution. This is precisely the difficulty that periodic pseudospectral codes were designed to remedy. But we have no “fast” transforms for the spherical Bessel functions that arise, and this limitation must be regarded as a trade-off against the geometric realism and the ease of satisfying boundary conditions. We further remark that difficult-

ties associated with singularities at $r = 0$ in spherical polar coordinates largely disappear when the C-K basis is used. We have noted this convenience previously in solutions to the two-dimensional Navier-Stokes equation inside a circle with no-slip boundaries [32, 33]. Furthermore, the code may be readily parallelized, there are no potential aliasing problems, and the accuracy with which the Galerkin approximations can preserve ideal invariants is a great advantage when attempting long-duration runs.

An outline of the paper is as follows. Section II introduces the expansion basis and shows how the nonlinear partial differential equations can be reduced to a set of ordinary differential equations for the expansion coefficients. We include a mention of the possible boundary conditions that could be introduced before settling on one set to illustrate the operation of the code. Some numerical subtleties are discussed in Section III. Sections IV and V illustrate the first applications of the code to some MHD problems we consider interesting and that are peculiar to spherical geometry. Section VI summarizes the results and discusses possible future applications of the method.

II. THE SPECTRAL DECOMPOSITION

C-K functions are constructed from a solution of the scalar Helmholtz equation:

$$(\nabla^2 + \lambda^2) \psi = 0, \quad (1)$$

where we are referring to spherical polar coordinates (r, θ, ϕ) and λ is an eigenvalue that will eventually be determined by boundary conditions. Vector eigenfunctions of the curl appropriate to spherical geometry may be constructed according to the recipe

$$\mathbf{J} = \lambda \nabla \times \mathbf{r} \psi + \nabla \times (\nabla \times \mathbf{r} \psi). \quad (2)$$

From this, it may readily be verified that $\nabla \times \mathbf{J} = \lambda \mathbf{J}$. Thus any single \mathbf{J} is a “force-free” or “Bernoulli” field, though the sum of two or more of them is not. The relevant scalar ψ is

$$\psi_{qlm} = C_{ql} j_l(|\lambda_{ql}|r) Y_{lm}(\theta, \phi). \quad (3)$$

Here, C_{ql} is a normalization constant, j_l is a spherical Bessel function of order l , and Y_{lm} is the normalized spherical harmonic expressed in terms of the polar angle θ and the azimuthal (longitudinal) angle ϕ . The number C_{ql} is chosen to make the volume integral of $\mathbf{J}_{qlm} \cdot \mathbf{J}_{qlm}^*$ over the computational domain equal to unity (the asterisk denotes complex conjugate). The explicit expression for C_{ql} in a sphere of radius R is

$$C_{ql} = |\lambda_{ql} j_{l+1}(|\lambda_{ql}|R)|^{-1} [l(l+1)R^3]^{-1/2}. \quad (4)$$

The integer l is $1, 2, 3, \dots$ and m runs in integer steps from $-l$ to l . An infinite sequence of values of λ_{ql} , labeled

by $q = 1, 2, 3, \dots$ and $q = -1, -2, -3, \dots$ is determined by an appropriate radial boundary condition on \mathbf{J} for a given l ; λ_{ql} may be positive or negative, and this determines the sign of the helicity of any given eigenfunction. Positive or negative q is to be associated with positive or negative λ_{ql} according to $\lambda_{-q,l} = -\lambda_{ql}$. For a variety of radial boundary conditions, the \mathbf{J}_{qlm} functions corresponding to differing indices q , l , or m can be shown to be orthogonal. Boundary conditions at two different radii can be imposed if spherical Neumann functions are also permitted in ψ . It is believed that the \mathbf{J} functions constitute a complete set for solenoidal vector functions, though the result has only been proved for cylindrical geometry.

Assuming the completeness of the C-K functions so defined, they are then appropriate for expanding various vector fields of incompressible MHD: the magnetic field, fluid velocity, vorticity, electric current density, and vector potential in the Coulomb gauge. We consider these to be the most important set of functions for spherical MHD and planetary dynamos in the class of problems we want to study. The ones of slowest spatial variation (smaller q , low l and m) contain the dipole and low-order multipole components of the fields and so, like Fourier series, provide a natural ordering of the spectral contributions from various spatial scales. The components of highest relative helicity are also included in these modes of least spatial variation. They may be matched on to external vacuum magnetostatic fields. In principle, they contain all the contributions to the fields from the largest spatial scales to the smallest; but unlike Fourier series, the larger spatial scales have a natural representation in the geometry of the physical system we wish to represent.

The MHD equations to be solved are, in familiar dimensionless (“Alfvénic”) units, an equation of motion for the fluid velocity \mathbf{v} ,

$$\frac{\partial \mathbf{v}}{\partial t} = \mathbf{v} \times \boldsymbol{\omega} + \mathbf{j} \times \mathbf{B} - \nabla \left(\mathcal{P} + \frac{v^2}{2} \right) + \nu \nabla^2 \mathbf{v} + \mathbf{f}, \quad (5)$$

and the induction equation for advancing the magnetic field \mathbf{B} ,

$$\frac{\partial \mathbf{B}}{\partial t} = \nabla \times (\mathbf{v} \times \mathbf{B}) + \eta \nabla^2 \mathbf{B}, \quad (6)$$

Here, \mathcal{P} is the dimensionless ratio of pressure to density (the mass density is assumed spatially uniform), and \mathbf{j} is the electric current density, $\mathbf{j} = \nabla \times \mathbf{B}$. A forcing function \mathbf{f} has been written on the right hand side of Eq. (5) to represent any externally applied mechanical force, a frequent convention in dynamo-motivated computations. Both \mathbf{B} and \mathbf{v} are divergenceless. The vorticity $\boldsymbol{\omega}$ is the curl of \mathbf{v} , and an evolution equation for it can be obtained by taking the curl of Eq. (5):

$$\frac{\partial \boldsymbol{\omega}}{\partial t} = \nabla \times (\mathbf{v} \times \boldsymbol{\omega}) + \nabla \times (\mathbf{j} \times \mathbf{B}) + \nu \nabla^2 \boldsymbol{\omega} + \nabla \times \mathbf{f}. \quad (7)$$

With appropriate boundary conditions, the vorticity $\boldsymbol{\omega}$ determines the velocity \mathbf{v} . The dimensionless viscosity

ν and magnetic diffusivity η can be interpreted, respectively, as reciprocals of kinetic and magnetic Reynolds numbers, where the relevant velocity might be the rms value of \mathbf{v} and the relevant length might be the energy-containing scale of \mathbf{v} (to be defined below).

The numerical scheme is to solve Eqs. (5) or (7) and (6) by representing \mathbf{v} and \mathbf{B} as the Galerkin expansions,

$$\mathbf{v}(\mathbf{r}, t) = \sum_{qlm} \frac{\xi_{qlm}^v(t)}{\lambda_{ql}} \mathbf{J}_{qlm}(\mathbf{r}) \quad (r \leq R) \quad (8)$$

$$\mathbf{B}(\mathbf{r}, t) = \sum_{qlm} \xi_{qlm}^B(t) \mathbf{J}_{qlm}(\mathbf{r}). \quad (9)$$

Here, the unknowns are the complex, time-dependent expansion coefficients ξ_{qlm}^v and ξ_{qlm}^B .

Next, we may substitute Eqs. (8) and (9) into Eqs. (6) and (7), say, and take inner products one at a time with the functions $\mathbf{J}_{q'l'm'}$. Using their orthonormality, the dynamical equations become

$$\frac{\partial \xi_i^v}{\partial t} = \sum_{j,k} (A_{jk}^i \xi_j^v \xi_k^v + B_{jk}^i \xi_j^B \xi_k^B) - \nu \lambda_i^2 \xi_i^v + \xi_i^f \quad (10)$$

$$\frac{\partial \xi_i^B}{\partial t} = \sum_{j,k} C_{jk}^i \xi_j^v \xi_k^v - \eta \lambda_i^2 \xi_i^B. \quad (11)$$

The indices i, j, k are regarded as shorthand; each one of them represents the triple of numbers q, l, m necessary to identify a single member of the family of the C-K functions \mathbf{J}_{qlm} . The sum is over all the values retained in the Galerkin expansion. As previously mentioned, the C-K functions will become orthogonal after imposing the boundary conditions. Boundary conditions different than the one studied here may also lead to an orthogonal set of \mathbf{J}_{qlm} .

The nonlinearities, both in the original partial differential equations and in the ordinary differential equations (10) and (11), are quadratic. The kinematic coupling coefficients (which do not contain the ξ) A_{jk}^i , B_{jk}^i , and C_{jk}^i , are numerical integrals of considerable complexity. Their evaluation and storage as a table is one of the most demanding parts of the computation, and some features of that evaluation are described in Section III. On the right hand side of Eq. (10), we have represented the forcing function \mathbf{f} , if any, by its expansion over the retained C-K functions. The coefficients ξ_i^f , if non-zero, are to be regarded as known, possibly time-dependent functions that may excite the velocity field, and may stand for a variety of possible mechanical processes.

It remains to specify the set of boundary conditions we are using, thereby determining the λ_{ql} . We demand that the radial components of \mathbf{v} , $\boldsymbol{\omega}$, \mathbf{B} , and \mathbf{j} shall vanish at the radius $r = R$. This boundary at $r = R$ is being regarded as a perfectly conducting spherical shell, coated on the inside with a very thin layer of insulating dielectric. It is impenetrable, as evidenced by the vanishing of the normal component of \mathbf{v} . The vanishing of the normal

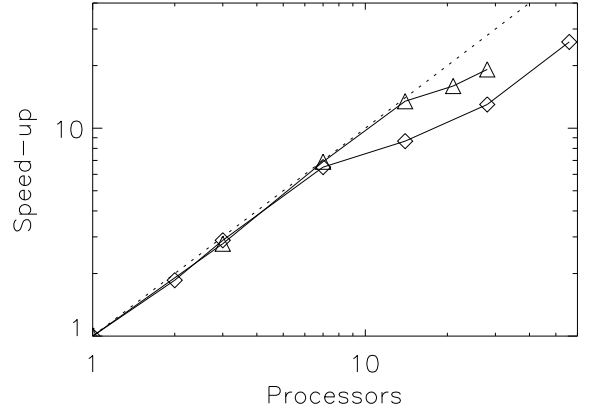


FIG. 1: Speed-up of the code in two Linux clusters in parallel simulations with $\max\{q\} = \max\{l\} = 7$. The dotted line indicates the ideal scaling.

component of $\boldsymbol{\omega}$ is implied by, but does not imply, no-slip boundary conditions on \mathbf{v} . It is a limitation of this method (and many others) that the satisfaction of no-slip boundary conditions introduces very complex considerations into the development. We consider that the fact that these complexities are present in much simpler problems and remain controversial there gives us license not to attempt no-slip boundaries in the present situation, though we mean to consider a variety of boundary conditions in later papers.

The vanishing of the normal components of all four of the vector fields, term by term, at $r = R$ is achieved by choosing the λ_{ql} so that

$$j_i(|\lambda_{ql}|R) = 0 \quad (12)$$

which determines the doubly-infinite sequence of λ_{ql} values. Each solution to Eq. (12) has associated with it the values λ_{ql} and $-\lambda_{ql}$. These will be distinguished by the choice of sign of the identifying index q .

With these boundary conditions, the coupling coefficients reduce to

$$A_{jk}^i = C_{jk}^i = \frac{\lambda_i}{\lambda_j} I_{jk}^i, \quad B_{jk}^i = \lambda_i \lambda_j I_{jk}^i, \quad (13)$$

where

$$I_{jk}^i = \int \mathbf{J}_i^* \cdot (\mathbf{J}_j \times \mathbf{J}_k) d^3x. \quad (14)$$

III. NUMERICAL METHOD

Equations (10) and (11) are solved numerically with double precision in a sphere of radius $R = 1$. The expansion coefficients ξ are in general complex, and since the fields are real, the coefficients satisfy the condition

$\xi_{q,l,-m} = (-1)^m \xi_{qlm}^*$. As a result, only the coefficients for non-negative values of m are stored and evolved in time.

Before the simulation is started, for a given resolution in q and l (and all possible values of m) all required values of the normalization coefficients C_{ql} are computed using Eq. (4) and stored. The values of λ_{ql} are computed numerically as the roots of the spherical Bessel functions [see Eq. (12)] using a combination of bisection and Newton-Raphson [34]. Finally, the coupling coefficients I_{jk}^i are computed and stored.

The coupling coefficients are complex, and from Eq. (14) satisfy the relation $I_{jk}^i = -I_{kj}^i$. The integral in Eq. (14) is separable in spherical coordinates. In the ϕ direction, the integral reduces to the condition $m_k = m_i - m_j$; in any other case the coupling coefficients I_{jk}^i are zero. The radial integral reduces to seven integrals involving three spherical Bessel functions or their derivatives, and the integral in the polar angle reduces to seven integrals on three Legendre functions and their derivatives. Radial integrals are computed numerically with high precision using Gauss-Legendre quadratures, while integrals in θ are computed using Gauss-Jacobi quadratures [34]. Due to symmetry properties of the Legendre functions, all coupling coefficients with $l_i + l_j + l_k + m_i + m_j + m_k$ even are purely real, while the remaining coefficients are purely imaginary, another property that can be used to save memory.

Once tables containing all these values are stored, the evolution of the system reduces to solving the set of ordinary differential equations defined by Eqs. (10) and (11). These equations are evolved using a Runge-Kutta method of fourth order [35]. The MHD equations have three quadratic ideal invariants: the total energy E , the magnetic helicity H , and the cross helicity K . In spectral space the invariants can be computed as

$$E = \frac{1}{2} \sum_i \left(\frac{|\xi_i^v|^2}{\lambda_i^2} + |\xi_i^B|^2 \right), \quad (15)$$

$$H = \frac{1}{2} \sum_i \frac{|\xi_i^B|^2}{\lambda_i}, \quad (16)$$

$$K = \frac{1}{2} \sum_i \frac{\xi_i^v \xi_i^{B*}}{\lambda_i}. \quad (17)$$

The conservation of these quantities up to the numerical precision serves as a test of the code and have been verified in simulations with $\nu = \eta = 0$. In a simulation with $\max\{q\} = \max\{l\} = 5$, the invariants were conserved up to the sixth decimal place after 200 turnover times. The turnover time is defined as $T = L/U$ where L is a characteristic length ($L \approx R = 1$ for these tests) and U is the rms velocity.

The system is evolved entirely in spectral space and all global quantities are also computed spectrally. To obtain representations of the fields in configuration space, Eqs. (8) and (9) are used.

The reciprocal of the smallest $|\lambda|$ may be identified

with the largest length scale in the dynamics allowed by the boundary conditions, and the reciprocal of the largest $|\lambda|$ retained may be considered to be the smallest resolvable spatial scale. In a typical computation (see e.g. Section V), these numbers may be ≈ 4.59 and ≈ 41.3 , respectively. The minimum and maximum wavenumbers in our previous 3D periodic dynamo computations (e.g. in a 256^3 dealiased simulation using the 2/3-rule [35]) have typically been 1 and 85 in dimensionless units, by comparison.

Besides the quadratic ideal invariants and the reconstruction of the field components, two vector quantities will be of interest. The angular momentum \mathbf{L} is defined as

$$\mathbf{L} = \int \mathbf{r} \times \mathbf{v} d^3x, \quad (18)$$

where a unity mass density is assumed, and the magnetic dipole moment $\boldsymbol{\mu}$ is given by

$$\boldsymbol{\mu} = \frac{1}{2} \int \mathbf{r} \times \mathbf{j} d^3x. \quad (19)$$

In terms of the C-K functions, these two quantities become

$$\mathbf{L} = 4R^3 \sqrt{\frac{\pi}{3}} \sum_q C_{q,1} \frac{j'_1(|\lambda_{q,1}|R)}{|\lambda_{q,1}|} \left[-\xi_{q,1,0}^v \hat{z} + \sqrt{2} \text{Re}(\xi_{q,1,1}^v) \hat{x} - \sqrt{2} \text{Im}(\xi_{q,1,1}^v) \hat{y} \right], \quad (20)$$

$$\boldsymbol{\mu} = 2R^3 \sqrt{\frac{\pi}{3}} \sum_q C_{q,1} |\lambda_{q,1}| j'_1(|\lambda_{q,1}|R) \left[-\xi_{q,1,0}^B \hat{z} + \sqrt{2} \text{Re}(\xi_{q,1,1}^B) \hat{x} - \sqrt{2} \text{Im}(\xi_{q,1,1}^B) \hat{y} \right]. \quad (21)$$

As previously mentioned, in the code a sphere with $R = 1$ is used. Note that only modes with $l = 1$ and $m = 0, \pm 1$ give a contribution to the angular momentum and the dipole moment. With the boundary conditions considered in this work, the angular momentum is not a conserved quantity unless $\nu = 0$. Other choices of the boundary conditions can lead to a conservation of the angular momentum even in the non-ideal case. Those boundary conditions apply to the case when the sphere of magnetofluid is isolated from torques, but we will defer consideration of that situation to a later paper.

The code is written in Fortran 90 and parallelized using MPI. Since most of the computing time is spent in the sums in Eqs. (10) and (11), the parallelization is done as follows. Each processor contains a complete copy of the expansion coefficients ξ , but only a portion of the coupling coefficients I_{jk}^i . The array I_{jk}^i is distributed in q if the number of processors is smaller or equal than $2q$, and distributed in q, l, m in any other case. Each processor computes the sums in Eqs. (10) and (11) locally for the corresponding values of q, l, m , and after each iteration of the Runge-Kutta method the coefficients ξ are

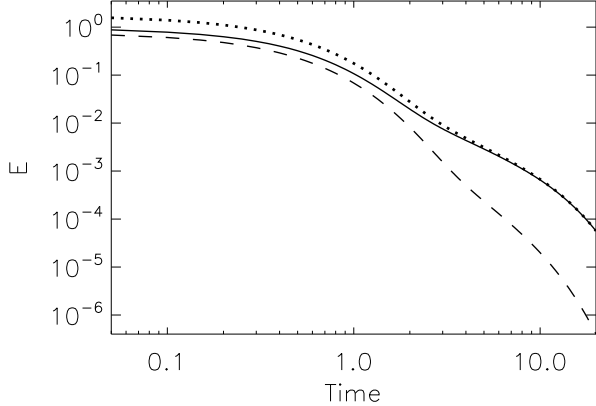


FIG. 2: Total energy (dotted line), magnetic energy (solid line), and kinetic energy (dashed line) as a function of time in run II. At late times the system is dominated by magnetic energy.

synchronized between all processors. The required communication is minimal and the scaling of the code as the number of processors is increased is close to ideal.

Figure 1 shows the speed-up vs. the number of processors in two different Linux clusters, in a simulation using $\max\{q\} = \max\{l\} = 7$. The clusters differ in the network configuration. The speed-up is defined as the time required to do one time step in N processors divided by the time required in one processor. The code shows ideal scaling up to $N \approx 2 \max\{q\}$. A drop is then observed and is related to the change in the parallel distribution of the array I_{jk}^i . However, after this drop a linear scaling is again recovered.

IV. SELECTIVE DECAY

Selective decay refers to a situation where an MHD system with some initial magnetic helicity evolves with a rapid decay of total energy relative to the magnetic helicity. The late-time state is a quasi-steady configuration in which the remaining energy is nearly all magnetic and is condensed into the longest wavelength modes allowed by the boundary conditions. Selective decay has been extensively studied in periodic boundary conditions (see, e.g., [36, 37, 38]). In Ref. [39] it was found that given isotropic initial conditions in a periodic box, the final state of the magnetic field corresponds to an Arn'old-Beltrami-Childress (ABC) field at the largest possible scale with A , B , and C equal. It is therefore of interest to test selective decay in a sphere, and to observe the geometry of the magnetic and velocity fields in the late-time state.

Two runs were done, the first (run I) with $\nu = \eta = 1 \times 10^{-2}$, and the second (run II) with $\nu = \eta = 6 \times 10^{-3}$. Run I was done with $\max\{q\} = \max\{l\} = 7$ (a total of

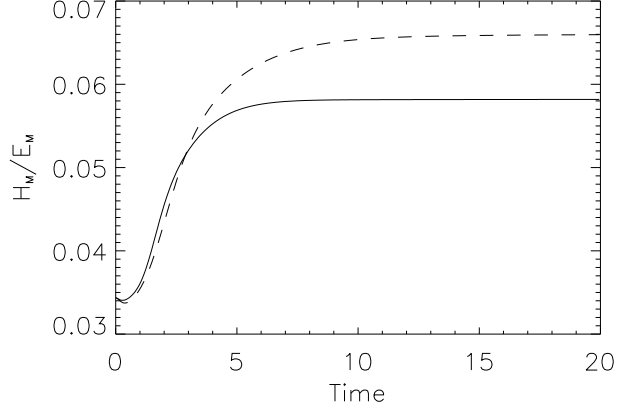


FIG. 3: Relative magnetic helicity as a function of time for runs I (solid line) and II (dashed line). The relative helicity at late times increases with the Reynolds number. Note the maximum possible value for the relative helicity is $\min^{-1}\{|\lambda|\} \approx 0.22$.

882 independent expansion coefficients), and run II with $\max\{q\} = \max\{l\} = 9$ (1620 expansion coefficients). In both simulations, no external force was applied, and the system was allowed to evolve for a long time (20 initial large scale turnover times).

The non-vanishing initial expansion coefficients in both simulations are

$$\xi_{3,3,0}^v = \xi_{-3,3,0}^v = -u_0, \quad \xi_{3,3,0}^B = \frac{5}{3} \xi_{-3,3,0}^B = B_0, \quad (22)$$

$$\xi_{3,3,m}^v = \xi_{-3,3,m}^v = u_0(1+i), \quad (23)$$

$$\xi_{3,3,m}^B = \frac{5}{3} \xi_{-3,3,m}^B = B_0(1-i), \quad (24)$$

where m runs from 1 to 3 and negative values of m are given by $\xi_{q,l,-m} = (-1)^m \xi_{qlm}^*$. The amplitudes u_0 and B_0 were chosen to have initial kinetic and magnetic energies of order unity ($u_0 = 4$ and $B_0 = 0.4$). These initial conditions correspond to a small cross correlation between the velocity and magnetic fields, a non-helical velocity field at an intermediate scale, and a (non-maximally) helical magnetic field at the same scale. The initial angular momentum is zero and remains negligible during the complete simulation. The kinetic and magnetic Reynolds numbers, based on the length $R = 1$ and the initial rms velocity, are respectively defined as

$$R_V = \frac{RU}{\nu}, \quad (25)$$

$$R_M = \frac{RU}{\eta}. \quad (26)$$

In run I $R_V = R_M \approx 98$, and in run II $R_V = R_M \approx 165$.

Figure 2 shows the time history of the kinetic, magnetic, and total energies in run II. At late times, the kinetic energy is negligible and the system is dominated by magnetic energy. The magnetic helicity decays slowly

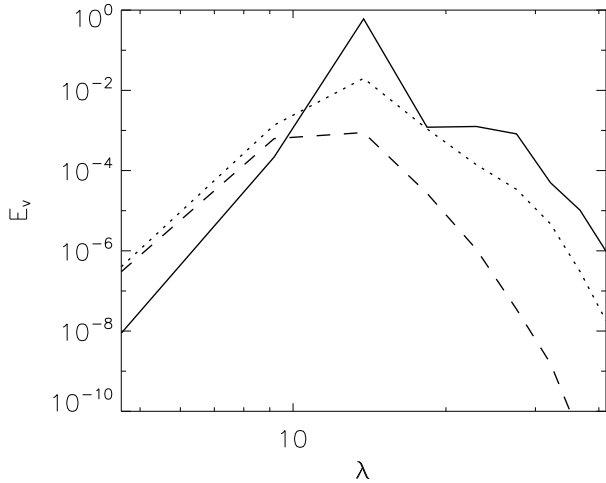


FIG. 4: Spectrum of kinetic energy as a function of λ for run II, at $t = 0.1$ (solid line), $t = 1.5$ (dotted line) and $t = 3$ (dashed line).

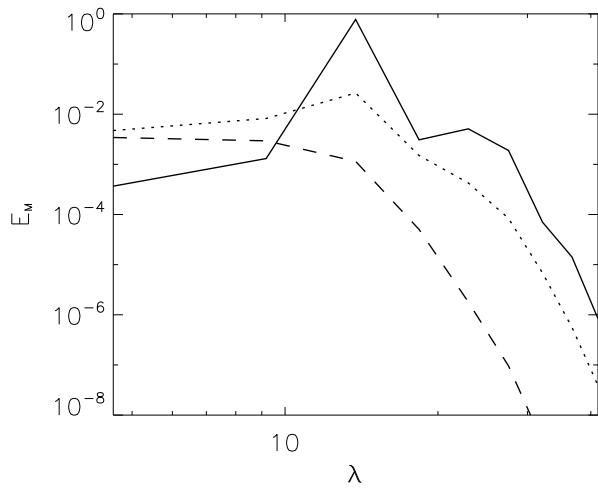


FIG. 5: Spectrum of magnetic energy as a function of λ for run II, at $t = 0.1$ (solid line), $t = 1.5$ (dotted line) and $t = 3$ (dashed line).

compared to the energy, as indicated by the evolution of the relative helicity H_M/E_M (Fig. 3). As time evolves, the ratio H_M/E_M increases until a steady state is reached. The final state reached by the system is not a “Taylor state”, a state of maximum possible helicity for the given energy (the maximum possible value for the relative helicity is $\min^{-1}\{|\lambda|\} \approx 0.22$). In run I, this is because after $t \approx 5$ most of the kinetic energy has decayed, and as a result the spectral exchange between modes stopped. In run II the decay of the kinetic energy takes place at a later time, and as a result the final value of the relative helicity is larger than in run I. Larger fi-

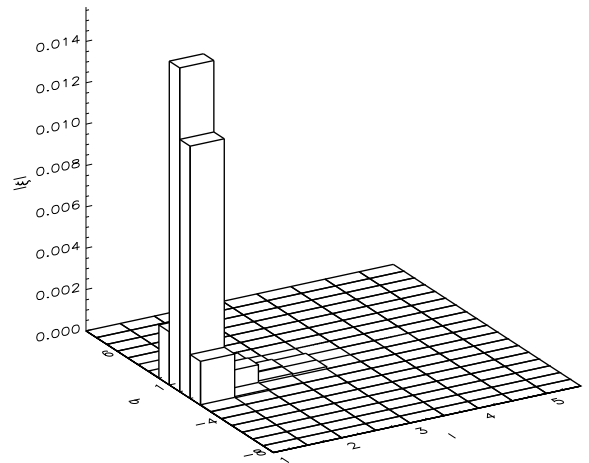


FIG. 6: Amplitude of the coefficients ξ^B in run II at $t = 10$ as a function of q and l (summed over all values of m). Most of the magnetic energy is at the largest available scale, and an asymmetry is observed between positive and negative values of q .

nal values of the relative helicity can be expected if the Reynolds numbers are further increased.

Since the C-K functions are eigenfunctions of the curl with eigenvalue λ , the Laplacian operators in the diffusion terms in Eqs. (5-7) are proportional to λ^2 . As a result, $|\lambda|$ plays in this case the role of the wavenumber k in the Fourier base. To define the energy spectrum, we linearly bin the spectral space in shells of constant $|\lambda|$ and sum the power of all the coefficients in each shell, in analogy with the usual procedure in Fourier-based spectral methods. Figures 4 and 5 show respectively the resulting kinetic and magnetic energy spectrum as a function of $|\lambda|$ in run II at three different times.

At early times ($t = 0.1$), the signature of the initial conditions in the spectrum can be easily recognized. Both spectra peak at $|\lambda| \approx 14$, corresponding to the non-vanishing initial perturbation at $q = 3$ and $l = 3$. As time evolves, the amplitude of the kinetic energy spectrum decays but the position of the peak remains approximately constant. On the other hand, the peak in the magnetic energy spectrum moves to smaller values of $|\lambda|$, corresponding to larger scales. At late times the system is dominated by magnetic energy, and most of it is concentrated in the largest available scale in the domain.

Based on the definition of the energy spectrum, we can also introduce an energy-containing lengthscale as

$$\ell = \frac{R \min\{|\lambda|\}}{E} \int E(|\lambda|) |\lambda|^{-1} d|\lambda|, \quad (27)$$

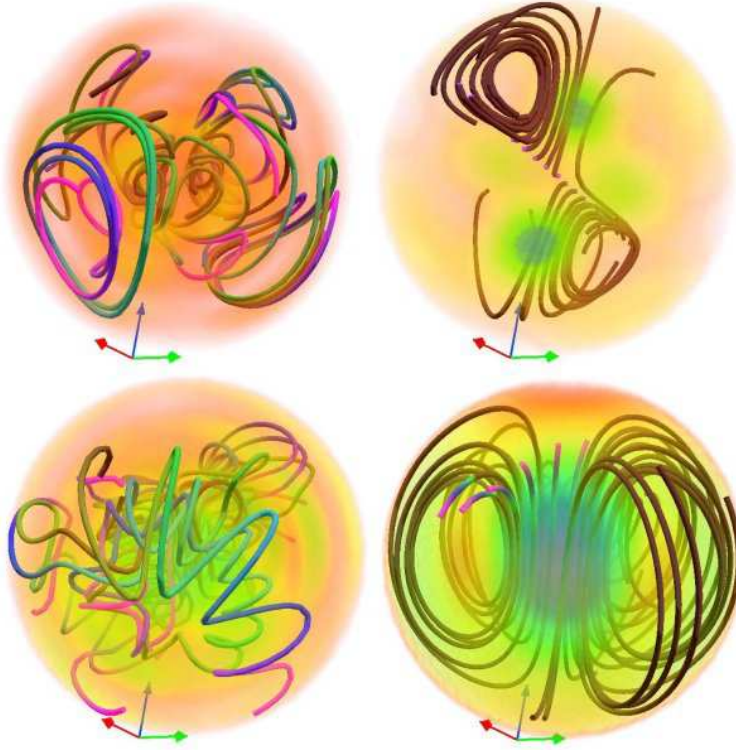


FIG. 7: Above: kinetic energy density and velocity field lines in run II, at $t = 1.5$ (left) and at $t = 15$ (right). Below: magnetic energy density and magnetic field lines in the same run, at $t = 1.5$ (left) and at $t = 15$ (right).

and a Taylor lengthscale

$$\lambda_T = R \min\{|\lambda|\} \left[E \left/ \int E(|\lambda|) |\lambda|^2 d|\lambda| \right. \right]^{1/2}, \quad (28)$$

where E is the energy, and $E(|\lambda|)$ is the energy spectrum as a function of $|\lambda|$ (the sums are represented symbolically as integrals). Using the kinetic and magnetic energies, these characteristic lengths can be computed for the velocity and magnetic fields. In both runs, at $t = 0$ $\ell \approx \lambda_T \approx 0.33$ for both fields. As the system evolves these quantities grow monotonically, but while at $t = 20$ for the velocity field $\ell \approx 0.5$, for the magnetic field $\ell \approx 1$. As a criterion to decide if the simulations were well resolved in spectral space, the scales where the kinetic and magnetic enstrophy spectrum peaked were observed as a function of time, and it was asked that their corresponding wavenumbers $|\lambda|$ were smaller than $\max\{|\lambda|\}$ at all times.

Figure 6 shows the amplitude of the individual modes ξ^B in run II at $t = 10$ as a function of q and l (all values of m for each value of l are summed). Most of the magnetic energy is concentrated in the shell with $l = 1$, and the modes with $q = \pm 1$ in this shell have the largest amplitude. Note the imbalance between the mode with $q = 1$ and $q = -1$, indicating some helicity is present in the magnetic field.

The dominance of a helical large scale magnetic field at late times can also be identified in an inspection of

the fields in configuration space. Figure 7 shows field intensity and a few field lines for the velocity and magnetic field at $t = 1.5$ (left) and $t = 15$ (right) in run II. While at early times both fields show small scale features, at late times the velocity field looks reminiscent of a quadrupole and the magnetic field looks like a dipole oriented roughly in the z direction. However, the magnetic field at $t = 15$ is helical and the magnetic field lines are not purely poloidal. There is a small toroidal component to the magnetic field, and the magnetic field lines proceed slowly in the ϕ -direction in a helical fashion.

In Fig. 7 and in the following visualizations the labels are as follows. The x , y , and z directions are indicated by the arrows (in the online version, these are respectively red, green, and blue). The fog opacity is proportional to the intensity of the field (in the online version, the intensity is also indicated by the fog color, with red, green, blue, and magenta from less intense to more intense). Field lines are computed taking a snapshot of the field at a fixed instant in time, and integrating a trajectory from four selected and fixed spatial points in the surroundings of the center of the sphere. The field is not evolved in time as the lines are integrated. To indicate the direction of the fields, in the online version the lines change color according to the distance integrated from the fixed initial point; from brown to dark green, dark blue, and dark magenta.

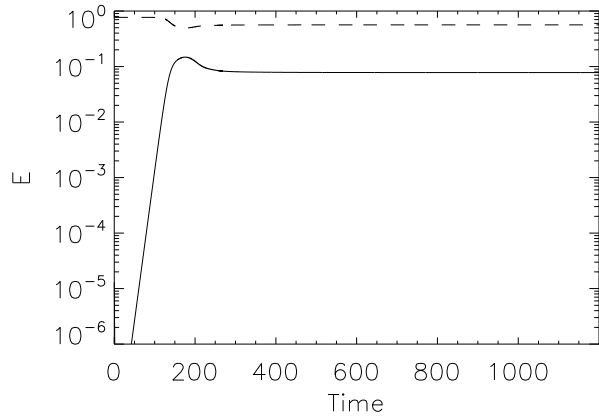


FIG. 8: Kinetic (dashed line) and magnetic energy (solid line) as a function of time in run III.

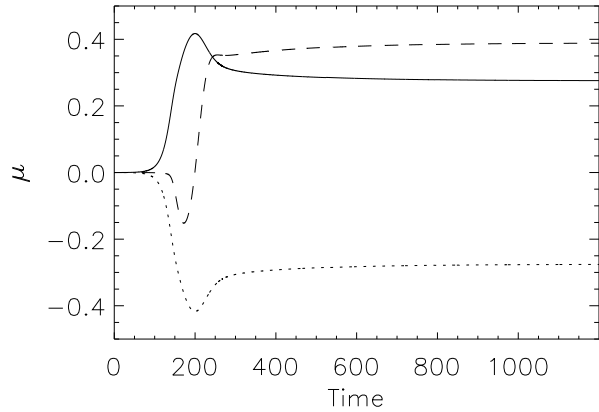


FIG. 9: Time evolution of the three components of the dipole moment in run III: x component (solid line), y (dotted line) and z (dashed line).

V. DYNAMO EFFECT

In a magnetohydrodynamic dynamo, a small magnetic field is amplified and sustained against Ohmic dissipation solely by the motions of a conducting fluid. As mentioned in the Introduction, magnetic fields observed in planets and stars are believed to be the result of a dynamo process. In this subsection, we study dynamo action in the sphere.

In the simulations discussed in this section, energy is injected in the system through the mechanical forcing \mathbf{f} in Eq. (5). In all cases, a hydrodynamic simulation was conducted first until reaching a steady state. The amplitude of the external forcing was chosen to have kinetic energy of order one in the steady state. Then, a random magnetic field with energy $E_M \approx 10^{-6}$ was loaded in the modes with $q = l = 4$. The simulations were continued to

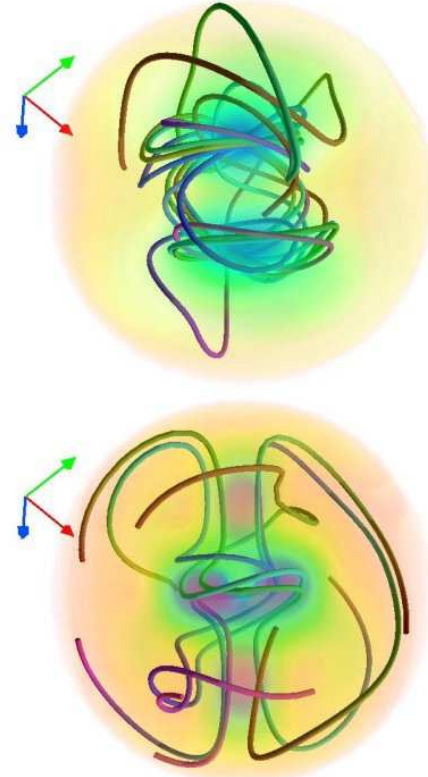


FIG. 10: Above: kinetic energy density and velocity field lines in run III, at $t = 915$. Below: magnetic energy density and magnetic field at the same time.

observe amplification of magnetic energy due to dynamo action.

Three dynamo simulations were done, in which the Reynolds numbers and the number of modes excited in the velocity field were progressively increased. We discuss first two simulations in which only a few modes were excited. While in the first case the system reaches a steady state with a stable dipole moment, in the second run the dipole spontaneously changes direction. Then, we finally present a dynamo computation where more modes are excited and the direction of the dipole moment changes erratically in time.

A resolution of $\max\{q\} = \max\{l\} = 9$ was used in all the runs. The same criteria than in the previous section was used to decide if a simulation was well resolved. For the last run, a simulation with higher resolution was also done to verify the results were not modified by the change in the resolution.

A. Laminar runs

In this section we present results from two runs with $\nu = \eta = 3 \times 10^{-3}$. In run III, the external forcing \mathbf{f} in

Eq. (5) is given by the coefficient

$$\xi_{2,2,1}^f = f_0(1+i), \quad (29)$$

with $f_0 = 1.4$, which corresponds to one C-K mode and as a result injects maximum kinetic helicity in the system. In run IV, the external forcing is

$$\xi_{2,2,0}^f = 5\xi_{-2,2,0}^f = f_0, \quad (30)$$

$$\xi_{2,2,m}^f = 5\xi_{-2,2,m}^f = f_0(1+i), \quad (31)$$

where m runs from 1 to 2 and negative values of m are again given by $\xi_{q,l,-m} = (-1)^m \xi_{qlm}^*$. The amplitude of the forcing is $f_0 = 0.9$. This forcing injects non-maximal kinetic helicity as well as kinetic energy into the system. The phase and amplitude of the external force \mathbf{f} were kept constant during the entire simulations.

Figure 8 shows the time history of the magnetic and kinetic energy in run III. The Reynolds numbers based on the length $R = 1$ and the rms velocity are $R_V = R_M \approx 290$, and the energy containing scale of the flow is $\ell \approx 0.5$. Before the magnetic field is introduced, only the forced mode is excited.

After the magnetic seed is introduced, the magnetic energy is amplified exponentially in a kinematic regime. Then the magnetic field saturates around $t \approx 150$ and the Lorentz force quenches the velocity field. In the final steady state, more mechanical modes besides the forced mode are excited. This is the result of an instability of the flow, triggered by the Lorentz force as the magnetic field grows exponentially.

Figure 9 shows time evolution of the three Cartesian components of the magnetic dipole moment in run III. The dipole moment grows during the kinematic regime, and after $t \approx 300$ the dipole seems to converge slowly to a steady state. Except for a small oscillation in the y component, no spontaneous change in the direction of $\boldsymbol{\mu}$ is observed.

A visualization of the velocity and magnetic fields in configuration space in the steady state of run III is shown in Fig. 10. The kinetic energy is concentrated in two counter-rotating regions, located in the center of each hemisphere. The velocity field in these regions is mostly toroidal, as indicated by the velocity field lines. The magnetic energy is larger in the center of the sphere, and along the axis defined by the two counter-rotating eddies. In the interior, but away from the axis, magnetic field lines are mostly toroidal, as the result of the stretching by the two counter-rotating eddies. Along the axis and close to the boundaries, the flow is mostly poloidal.

The time history of the kinetic and magnetic energy in run IV is shown in Fig. 11. The Reynolds numbers for this run are $R_V = R_M \approx 280$, and the energy containing scale of the flow is $\ell \approx 0.48$. Although the kinematic viscosity and magnetic diffusivity are the same as in run III, the external forcing injects energy in a larger number of modes and even before the magnetic field is introduced non-forced modes have some mechanical energy.

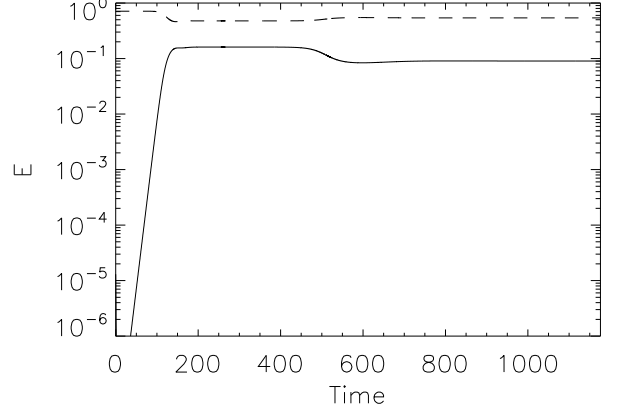


FIG. 11: Kinetic (dashed line) and magnetic energy (solid line) as a function of time in run IV.

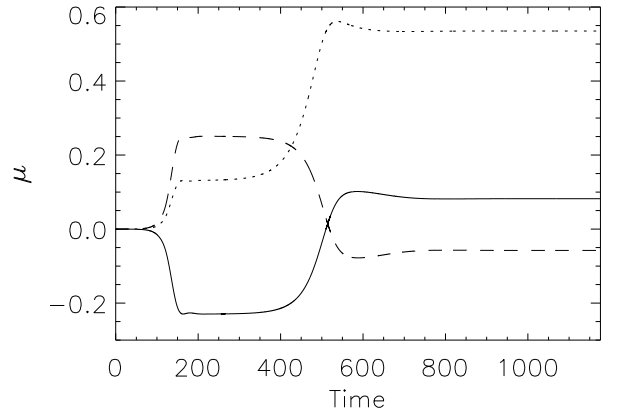


FIG. 12: Time evolution of the three components of the dipole moment in run IV. Same labels as in Fig. 9.

After the magnetic seed is introduced, the magnetic energy grows exponentially until at $t \approx 150$ saturates. The system seems to reach a steady state but suddenly at $t \approx 500$ the magnetic energy decreases by a factor of ≈ 1.8 , the kinetic energy increases by ≈ 1.1 , and the system reaches a second steady state.

The abrupt change in the kinetic and magnetic energy in run IV at $t \approx 500$ is associated with a reorientation of the magnetic dipole moment. Figure 12 shows the time evolution of the three components of the magnetic dipole moment. In the kinematic stage the dipole moment grows until reaching a first quasi-steady state. The components of the dipole moment are approximately constant until at $t \approx 500$ the magnetic field evolves rapidly to a second attractor and the dipole moment changes direction. The angle the dipole flips by is close to $\pi/2$. The amplitude of the dipole moment also changes as the dipole shifts; while at $t \approx 300$ $|\boldsymbol{\mu}| \approx 0.36$, at $t \approx 1000$ $|\boldsymbol{\mu}| \approx 0.54$.

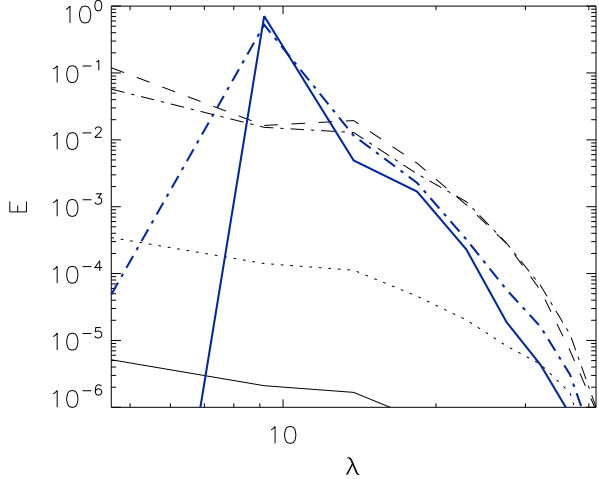


FIG. 13: Kinetic energy spectrum at $t = 52$ [thick (blue) solid line] and at $t = 500$ [thick (blue) dash-dotted line] in run IV; the thin lines correspond to the magnetic energy spectrum at $t = 52$ (solid), $t = 82$ (dotted), $t = 250$ (dashed), and $t = 500$ (dash-dotted).

Figure 13 shows the kinetic and magnetic energy spectra in run IV at different times. The kinetic energy spectrum peaks at $|\lambda| \approx 9$, corresponding to the forced modes with $q = 2$ and $l = 2$. The energy in the remaining modes is at least two orders of magnitude smaller than in the forced modes. At late times, some kinetic energy is excited in the largest available scale, as well as a small angular momentum ($|\mathbf{L}|^2/E_V \approx 1.5 \times 10^{-4}$ after $t \approx 600$). The angle between the dipole moment and this small angular momentum remains constant after $t = 100$ and is $\pi/2$. Visualizations of the velocity and magnetic fields in configuration space are shown in Fig. 14. The geometry of the velocity field is more complex than in run III. Note at $t = 315$ the magnetic field lines are mostly poloidal in the center of the sphere, and toroidal close to the boundary.

B. A chaotic simulation

In run V the external forcing \mathbf{f} is given by Eqs. (30,31), but the kinematic viscosity and magnetic diffusivity are $\nu = \eta = 3 \times 10^{-4}$. The kinetic and magnetic Reynolds numbers are $R_V = R_M \approx 2300$, and the energy-containing and Taylor scales are respectively $\ell \approx 0.4$ and $\lambda_T = 0.35$.

The evolution of the kinetic and magnetic energy in run V is shown in Fig. 15. Again, after an initial kinematic regime where the magnetic energy is amplified exponentially, the system reaches a statistical steady state. Note that in this simulation both the kinetic and magnetic energy fluctuate strongly with time, indicating the nonlinear coupling between modes is stronger than in runs

III and IV, as a result of the higher Reynolds numbers.

Figure 16 shows the time evolution of the three Cartesian components of the dipole moment in run V. All components of $\boldsymbol{\mu}$ fluctuate randomly, and change sign with a characteristic time of the order of 100 turnover times. The angular momentum is small, and fluctuates around $|\mathbf{L}|^2/E_V \approx 5 \times 10^{-3}$. However, unlike run III, in this simulation the angle between the dipole moment and the angular momentum is not constant and fluctuates randomly between 0 and π . In previous studies of α^2 geodynamo, it was found that the α effect favors an equatorial dipole field [40], and it was shown that small scale fluctuations can give an axial dipole. The results in Ref. [40] were obtained for kinematic simulations, while the alignment observed here is for the nonlinear MHD regime. This point deserves further study in simulations with larger angular momentum.

The kinetic and magnetic energy spectra in run V at several times are shown in Fig. 17. More modes are excited in the velocity field, in accordance with the strong fluctuations in time observed in the kinetic energy. While in runs III and IV the magnetic energy spectrum peaks at large scales even during the kinematic regime, in run V at early times the magnetic energy peaks at scales smaller than the forcing scale. Also, after the nonlinear saturation of the dynamo, a fluctuation in the amplitude of the large scale magnetic field is observed. The minima are correlated with times of minima of μ^2 , when the three components of the dipole moment fluctuate around zero. Most of the activity in this run is in small scales and fluctuations in the flow are larger than in runs III and IV. Even at late times when a large scale magnetic field has developed, intermediate scales give a large contribution to the magnetic energy. This also explains the strong fluctuations observed in the dipole moment. Since $\boldsymbol{\mu}$ is proportional to the current density, the small scales give a large contribution to the dipole moment.

Figure 18 shows the magnetic and velocity field in real space at two different times in run IV. The fields have more small scale structure than in run III. Also, in the kinematic regime (see e.g. the magnetic field at $t = 75$) the magnetic energy is mostly in the small scales, as also indicated by the magnetic energy spectrum.

VI. DISCUSSION

We have provided some computational machinery that is intended to open a quantitative discussion of nonlinear magnetohydrodynamics inside a rigid sphere, for essentially arbitrary parameter ranges and initial conditions. The attempt is to be distinguished both from previous computations of magnetic dynamo processes in rectangular periodic boundary conditions, where material boundaries are not involved, and from those geo-dynamo computations whose main goal is a numerical reproduction of the Earth's magnetic field behavior. We are interested in the physical processes involved in the mechanical excita-

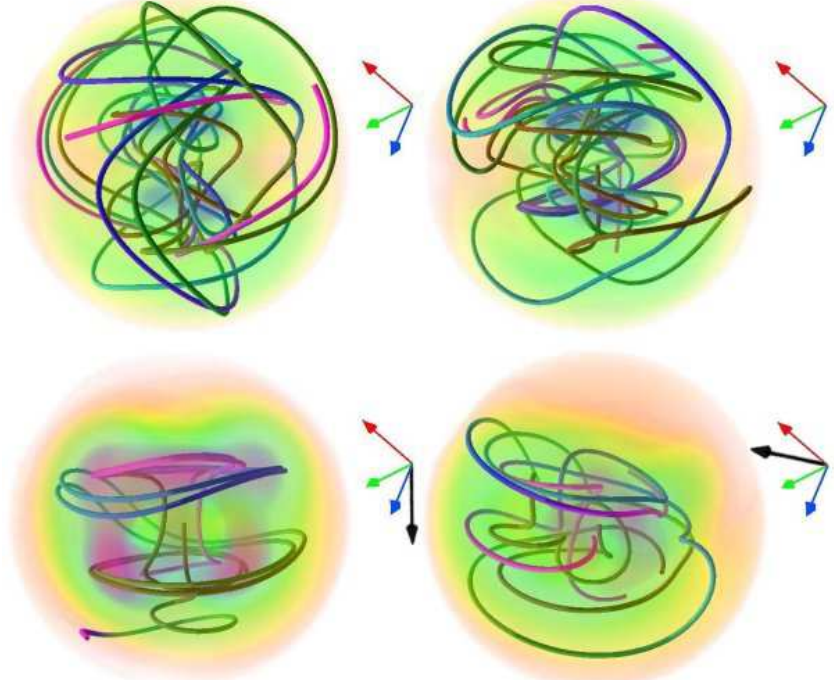


FIG. 14: Above: kinetic energy density and velocity field lines in run IV, at $t = 315$ (left) and at $t = 1065$ (right). Below: magnetic energy density and magnetic field lines in the same run, at $t = 315$ (left) and at $t = 1065$ (right). The black arrows indicate the direction of the dipole moment.

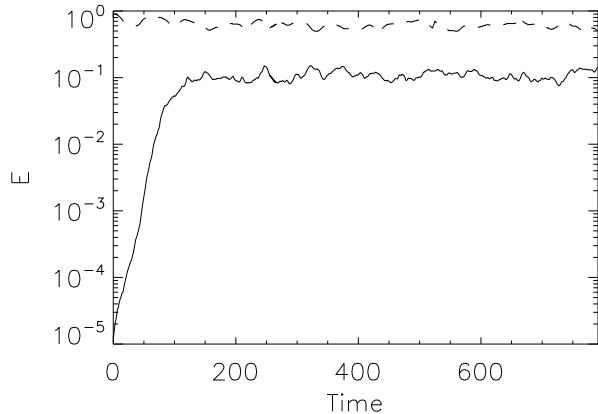


FIG. 15: Kinetic (dashed line) and magnetic energy (solid line) as a function of time in run V.

tion of magnetic fields in spherically-bounded electrically conducting fluids. In addition to the spherical geometry, there are also other features that become important, such as angular momentum, rotation of the boundary (omitted here, the inclusion of rotation is intended in future investigations), and different types of mechanical excitations. The pathway is also open to the inclusion of differentially rotating inner solid cores with the addition

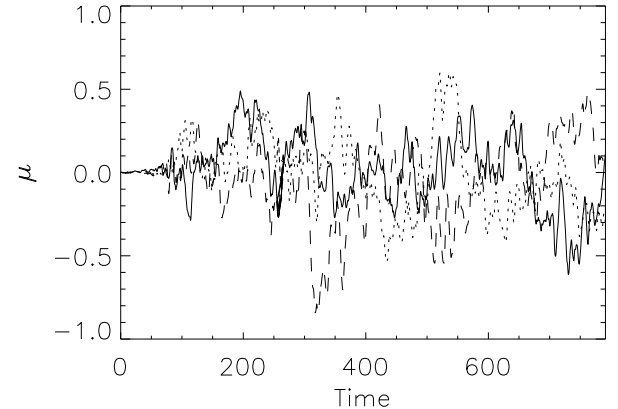


FIG. 16: Time evolution of the three components of the dipole moment in run V. Labels are as in Fig. 9. Note that the x and z components are out of phase and change sign approximately at the same time, while the y component seems to be fluctuating around zero.

of spherical Neumann functions into Eq. (3).

The operation of the wholly spectral code, which had a precedent in periodic circular-cylinder geometry, has been illustrated by two examples: “decay” turbulence computations in which relaxation to a helical magnetic state with negligible kinetic energy has been observed,

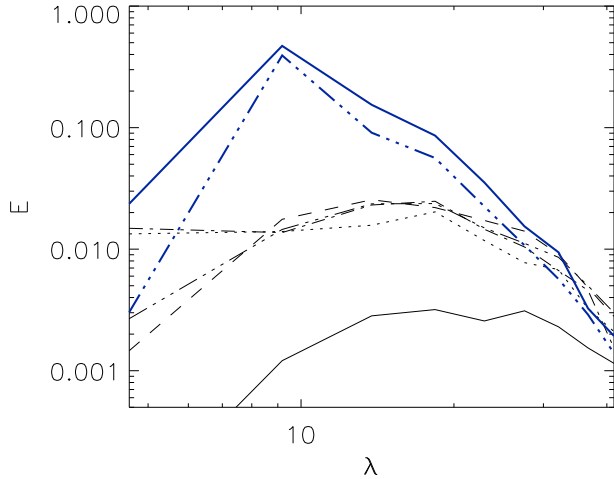


FIG. 17: Kinetic energy spectrum at $t = 75$ [thick (blue) solid line] and at $t = 600$ [thick (blue) dash-triple dotted line] in run V; the thin lines correspond to the magnetic energy spectrum at $t = 75$ (solid), $t = 168$ (dotted), $t = 240$ (dashed), $t = 544$ (dash-dotted), and $t = 500$ (dash-triple dotted).

and “dynamo” computations that have been performed by mechanically driving the velocity field, resulting in the generation of magnetic energy and a magnetic dipole moment. The dipole moment, unregulated by the inclusion of either rotation or possible thermally convective rolls with a preferred orientation, has been seen

to “flip,” spontaneously changing direction at an unpredictable time. Under these circumstances, the change in orientation of the dipole moment appears to be an easily achievable process: it has happened virtually every time we have tried it if some fluctuations were present in the velocity field. Its ease of achievement, in relation to the level of turbulence it occurs in, and its possible restriction by the effects of rotation and/or large net angular momentum (they are not the same thing) remain to be investigated. It is our plan to continue to study this problem, putting in new effects and boundary modifications in an attempt to understand them one at a time, even though one knows that in the planetary dynamo problem, they are likely to all be present at once. We have also done relatively little exploration of the effects of different kinds of forcing mechanisms on the form of the magnetic fields generated, and that, too, needs further consideration.

Acknowledgments

The authors would like to express their gratitude to A. Pouquet for valuable discussions and his careful reading of the manuscript. Computer time was provided by NCAR. The NSF grants CMG-0327888 at NCAR and ATM-0327533 at Dartmouth College supported this work in part and are gratefully acknowledged. Three-dimensional visualizations of the flow were done using VAPoR [41], a software for interactive visualization and analysis of large datasets.

[1] H. K. Moffatt, *Magnetic field generation in electrically conducting fluids*, Cambridge Univ. Press, Cambridge, 1978.

[2] G. A. Glatzmaier and P. H. Roberts, *Nature* **377**, 203 (1995).

[3] M. Dikpati and P. Charbonneau, *Astrophys. J.* **518**, 508 (1999).

[4] M. Kono and P. H. Roberts, *Rev. Geophys.* **40**, 1 (2002).

[5] D. Nandy and A. R. Choudhuri, *Science* **296**, 1671 (2002).

[6] P. D. Mininni and D. O. Gómez, *Astron. Astrophys.* **426**, 1065 (2004).

[7] A. Gailitis, O. Lielausis, E. Platacis, S. Dement'ev, A. Cifersons, G. Gerbeth, T. Gundrum, F. Stefani, M. Christen, and G. Will, *Phys. Rev. Lett.* **86**, 003024 (2001).

[8] R. Steiglitz and U. Müller, *Phys. Fluids* **13**, 561 (2001).

[9] K. Noguchi, V. I. Pariev, S. A. Colgate, H. F. Beckley, and J. Nordhaus, *Astrophys. J.* **575**, 1151 (2002).

[10] F. Pétrélis, M. Bourgoin, L. Marié, J. Burguete, A. Chiffaudel, F. Daviaud, S. Fauve, P. Odier, and J.-F. Pinton, *Phys. Rev. Lett.* **90**, 174501 (2003).

[11] D. R. Sisan, W. L. Shew, and D. P. Lathrop, *Phys. Earth Plan. Int.* **135**, 137 (2003).

[12] E. J. Spence, C. B. Forest, M. D. Nornberg, and R. D. Kendrick, Observation of a turbulence-generated large scale magnetic field, *Submitted to Phys. Rev. Lett.*

[13] P. H. Roberts and G. A. Glatzmaier, *Geophys. Astrophys. Fluid Dyn.* **94**, 47 (2001).

[14] A. Brandenburg and K. Subramanian, *Phys. Rep.* **417**, 1 (2005).

[15] P. Charbonneau, *Living Rev. Solar Phys.* **2** (2005), <http://www.livingreviews.org/lrsp-2005-2>.

[16] Y. Ponty, P. D. Mininni, D. C. Montgomery, J.-F. Pinton, H. Politano, and A. Pouquet, *Phys. Rev. Lett.* **94**, 164502 (2005).

[17] P. D. Mininni, Y. Ponty, D. C. Montgomery, J.-F. Pinton, H. Politano, and A. Pouquet, *Astrophys. J.* **626**, 853 (2005).

[18] P. D. Mininni and D. C. Montgomery, *Phys. Rev. E* **72**, 056320 (2005).

[19] A. Alexakis, P. D. Mininni, and A. Pouquet, *Phys. Rev. E* **72**, 046301 (2005).

[20] P. D. Mininni, A. Alexakis, and A. Pouquet, *Phys. Rev. E* **72**, 046302 (2005).

[21] G. A. Glatzmaier and P. H. Roberts, *Science* **274**, 1887 (1996).

[22] S. Chandrasekhar and P. C. Kendall, *Astrophys. J.* **126**, 457 (1957).

[23] L. Turner, *Ann. Phys.* **149**, 58 (1983).

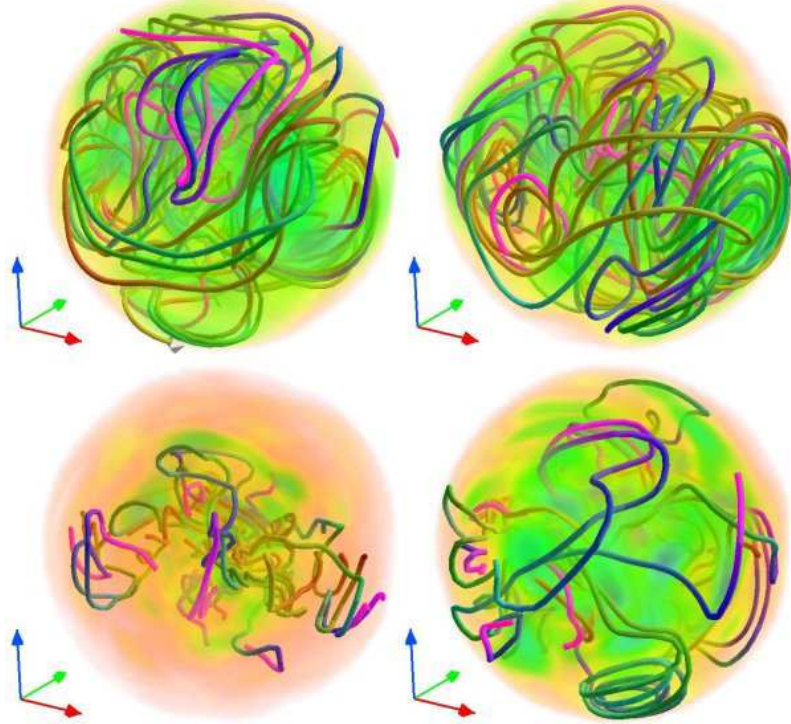


FIG. 18: Above: kinetic energy density and velocity field lines in run IV, at $t = 75$ (left) and at $t = 1035$ (right). Below: magnetic energy density and magnetic field lines in the same run, at $t = 75$ (left) and at $t = 1035$ (right).

- [24] Z. Yoshida, *Prog. Theor. Phys.* **86**, 45 (1991).
- [25] Z. Yoshida, *J. Math. Phys.* **33**, 1252 (1992).
- [26] J. Cantarella, D. DeTurck, H. Gluck, and M. Teytel, *Phys. Plasmas* **7**, 2766 (2000).
- [27] D. C. Montgomery, L. Turner, and G. Vahala, *Phys. Fluids* **21**, 757 (1978).
- [28] X. W. Shan, D. Montgomery, and H. D. Chen, *Phys. Rev. A* **44**, 6800 (1991).
- [29] X. W. Shan and D. Montgomery, *Plasma Phys. Cont. Fus.* **35**, 619 (1993).
- [30] X. W. Shan and D. Montgomery, *Plasma Phys. Cont. Fus.* **35**, 1019 (1993).
- [31] X. W. Shan and D. Montgomery, *Phys. Rev. Lett.* **73**, 1624 (1994).
- [32] S. J. Li and D. Montgomery, *Phys. Lett. A* **218**, 281 (1996).
- [33] S. J. Li, D. Montgomery, and W. B. Jones, *Theor. Comp. Fluid Dyn.* **9**, 167 (1997).
- [34] W. H. Press, B. P. Flannery, S. A. Teukolsky, and W. T. Vetterling, *Numerical Recipes in FORTRAN 77*, Cambridge Univ. Press, Cambridge, 1992.
- [35] C. Canuto, Y. Hussaini, A. Quarteroni, and T. Zang, *Spectral methods in fluid dynamics*, Springer Verlag, New York, 1988.
- [36] W. H. Matthaeus and D. Montgomery, *Ann. N. Y. Acad. Sci.* **357**, 203 (1980).
- [37] A. C. Ting, W. H. Matthaeus, and D. Montgomery, *Phys. Fluids* **29**, 3261 (1986).
- [38] R. Kinney, J. C. McWilliams, and T. Tajima, *Phys. Plasmas* **2**, 3623 (1995).
- [39] P. D. Mininni, D. C. Montgomery, and A. Pouquet, *Phys. Rev. E* **71**, 046304 (2005).
- [40] A. Tilgner, *Geophys. Astrophys. Fluid Dyn.* **98**, 225 (2004).
- [41] J. Clyne and M. Rast, A prototype discovery environment for analyzing and visualizing terascale turbulent fluid flow simulations, in *Visualization and data analysis 2005*, edited by R. F. Erbacher, J. C. Roberts, M. T. Grohn, and K. Borner, pp. 284–294, Bellingham, Wash., 2005, SPIE, <http://www.vapor.ucar.edu>.